

A Large-Eddy Simulation Study of Thermal Effects on Turbulence Coherent Structures in and above a Building Array

SEUNG-BU PARK AND JONG-JIN BAIK

School of Earth and Environmental Sciences, Seoul National University, Seoul, South Korea

(Manuscript received 28 June 2012, in final form 4 January 2013)

ABSTRACT

Thermal effects on turbulent flow in and above a cubical building array are numerically investigated using the parallelized large-eddy simulation model (PALM). Two cases (no heating and bottom heating) are simulated and are compared with each other, focusing on thermal effects on turbulence coherent structures. In the no-heating case, the streaky or streamwise-elongated structures of low-speed regions appear above the building array and ejections in the low-speed regions play an important role in transporting momentum downward. In the bottom-heating case, plume-shaped structures appear with streamwise-elongated structures and the magnitude of vertical turbulent momentum flux averaged over the low-speed regions increases. Elliptical structures of negative streamwise velocity perturbation and vortical structures similar to hairpin vortices appear above the building array in the conditionally averaged fields in both cases, and the coherent structures expand more vertically when the bottom is heated. At or just above the rooftop height, high-speed streaks are distinct and sweeps induced by the streaks or shear instability are important for momentum transport in both cases. In the bottom-heating case, the magnitude of vertical turbulent momentum flux at the tops of cavity spaces increases, partly owing to the strengthened ejections. Below the rooftop height, the high-speed streaks occasionally enter intersection spaces and induce spanwise diverging flow there in both cases. When the bottom is heated, intensified updrafts induce more organized secondary circular flow and the spanwise flow in the building array is strengthened by the secondary flow.

1. Introduction

Turbulent flow in urban areas has become a central issue in urban boundary layer meteorology because of its importance in the transport processes of momentum, heat, and pollutants. However, turbulent flow in urban areas is quite complex because of its inherent nature (e.g., intermittency), various shapes and arrangements of buildings, building surface or street bottom heating, etc. Many previous studies have focused on the mean and statistical features of turbulent flow in and above idealized building arrays through wind-tunnel experiments and numerical simulations (Brown et al. 2001; Cheng and Castro 2002; Kim and Baik 2004; Castro et al. 2006; Santiago et al. 2007). Although the mean and statistical features of turbulent flow have been fairly well investigated by these studies, our understanding of the transport processes is still not sufficient because turbulent

flow accompanying transport processes is intermittent and not always random. In fact, particular structures known as coherent structures or organized structures appear repeatedly in the turbulent boundary layer and they play an important role in the transport processes, as reported by Robinson (1991) and Rossi et al. (2010).

Kanda et al. (2004) and Kanda (2006) conducted large-eddy simulations (LES) of turbulent flow over building arrays and investigated the characteristics of coherent structures. Both of these studies showed that the streaky structures of low-speed regions and the streamwise vortices appear above the building arrays and that the coherent structures resemble those of smooth wall boundary layers. Coceal et al. (2007) proposed a conceptual model of unsteady turbulent flow in and above a staggered building array, based on direct numerical simulation results. According to the conceptual model, coherent structures that appear above the building array resemble well-known structures (e.g., hairpin vortices) that occur in smooth wall boundary layers and they interact with shear layer structures shed off the tops of buildings. Inagaki and Kanda (2010) analyzed observed data from an outdoor scale model experiment. They found

Corresponding author address: Jong-Jin Baik, School of Earth and Environmental Sciences, Seoul National University, Seoul 151-742, South Korea.
E-mail: jjbaik@snu.ac.kr

that spatially filtered structures are composed of large streaks of low-speed regions and substructures on the streaks and that the substructures are a main cause of ejections. Recently, based on LES results, Inagaki et al. (2012) reported that the coherent structures of velocity and temperature fields in a building array are closely related to the turbulence organized structures above them such as low-speed streaks. They classified the instantaneous flow patterns in a cavity into cavity-eddy and flushing events, and flushing events occur frequently beneath the low-speed streaks. Despite these insightful studies, it remains unclear how coherent structures above building arrays interact with turbulent flow in building arrays. Furthermore, previous studies have not focused on thermal effects on coherent structures. Surface heating is one of the main sources of turbulence in urban areas (Christen et al. 2009), and it can affect coherent structures and transport processes.

In this study, we investigate turbulent flow structures in and above a building array in neutrally and unstably stratified environments, focusing on thermal effects on coherent structures. In section 2, the LES model and simulation setup are described. The LES model is validated in section 3. Simulation results are presented and discussed in section 4. A summary and conclusions are given in section 5.

2. Model description and simulation setup

In this study, the parallelized LES model (PALM) developed at the Leibniz University of Hannover (Raasch and Schröter 2001; Letzel et al. 2008) is used to simulate turbulent flow in and above a building array. The governing equations in PALM are implicitly filtered Boussinesq equations. The momentum equation, thermodynamic energy equation, and subgrid-scale (SGS) turbulent kinetic energy (TKE) equation are numerically solved using the third-order Runge–Kutta scheme for time integration and the second-order Piacsek and Williams (1970) scheme for advection. The SGS turbulent fluxes are parameterized using the 1.5-order Deardorff (1980) scheme that uses SGS TKE to calculate eddy viscosity. More details of PALM can be found in Letzel et al. (2008).

Figure 1a shows the computational domain and building configuration. The computational domain size is 480 m in the x direction (streamwise direction), 480 m in the y direction (spanwise direction), and 550 m in the z direction (vertical direction). The grid size in both the x and y directions is 1 m (much larger than the estimated Kolmogorov scale ~ 1 mm). The grid size in the z direction is uniform at 1 m up to $z = 100$ m and then gradually increases with an expansion ratio of 1.08. An idealized building array composed of same-sized cubical buildings

(20 m height) is considered. The cubical buildings are arranged in lines with a constant spacing of 20 m in both the x and y directions. Therefore, the plan area density of the building array is 25% and the aspect ratio of the street canyon is one, with a skimming flow regime occurring in the building array (Macdonald et al. 1997).

Considering that the building arrays with the same geometry are repeated in both the x and y directions, the cyclic boundary condition is applied at the lateral boundaries for velocity components, SGS TKE, and temperature. The zero-gradient boundary condition is applied at the top boundary. The initial ambient wind blows in the x direction, and its vertical profile is logarithmic. Flow in the computational domain is driven by a constant external pressure gradient in the x direction, and the Coriolis effect is not included in this study. At the grid points closest to all the solid surfaces, the Monin–Obukhov (MO) similarity is employed in the momentum equation and thermodynamic energy equation.

Two simulations are conducted to investigate thermal effects on turbulent flow: no-heating (NH) case and street bottom-heating (BH) case. The temperature of the street bottom is set to be 10 K higher than that of the initial ambient air, and the bulk Richardson number in the BH case is -0.31 . The bulk Richardson number is defined as $R_b = [2gH(T_{2H} - T_0)]/(T_{2H}U_{2H}^2)$, where H is the building height; T_{2H} and U_{2H} are the temperature and streamwise wind speed at $z = 2H$, respectively; T_0 is the temperature of the heated street bottom; and g is the gravitational acceleration. PALM is integrated for 4.5 h in the NH case, and the last 30 min of simulation data are used for analysis. Then, PALM is integrated for 1 h more with the street bottom being heated. Also in the BH case, the last 30 min of simulation data are analyzed.

3. Validation

The LES model is validated using the wind-tunnel data of Uehara et al. (2000). Figure 2 shows the vertical profiles of normalized streamwise velocity and normalized temperature at the center of a street canyon in the numerical simulation and wind-tunnel experiment. As in the wind-tunnel experiment, an array of cubical buildings is considered in the numerical simulation and the street width in the x direction is equal to the building height and the street width in the y direction is equal to half the building height. Turbulent flow in and above the building array for each of the isothermal (neutral) and bottom-heated (unstable) cases is simulated. In the unstable case, the temperature of the bottom is adjusted to be 13 K higher than that of the ambient air to set the bulk Richardson number of the numerical simulation similar to that of the wind-tunnel experiment ($R_b = -0.21$).

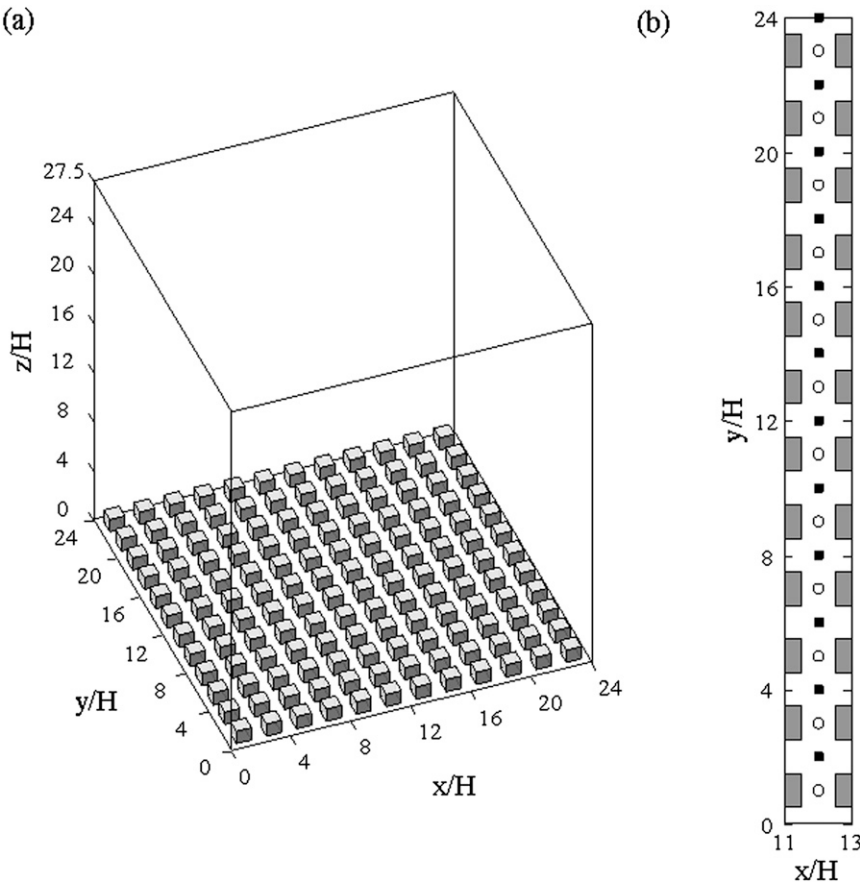


FIG. 1. Illustrations of (a) the computational domain and building configuration and (b) the sampling points of the vertical profiles in Fig. 3; H is the building height.

In the numerical simulation and wind-tunnel experiment, the magnitude of normalized streamwise velocity in the unstable case is larger than that in the neutral case in and above the building array. Although there are some discrepancies in the magnitude of normalized streamwise velocity, the LES model properly simulates the strengthened vortex circulation in the bottom-heated street canyon. Moreover, the vertical profile of normalized temperature in the numerical simulation is in good agreement with that in the wind-tunnel experiment.

4. Results and discussion

a. Vertical profiles

Figure 3 shows the vertical profiles of 12 points-averaged mean streamwise velocity \bar{u} , vertical turbulent momentum flux $\bar{u'w'}$, root-mean-square (RMS) of streamwise velocity perturbation $\sqrt{\bar{u'^2}}$, and RMS of vertical velocity perturbation $\sqrt{\bar{w'^2}}$. Here, u' and w' denote deviations from the time-averaged velocity components \bar{u} and \bar{w} , respectively. SGS parts are not included in

the calculated turbulence statistics because their magnitudes are much smaller than the magnitudes of resolved parts. For example, the ratio of SGS TKE to resolved TKE is smaller than ~ 0.12 . To investigate the positional dependency of turbulence statistics, we divide the space ($11.5 \leq x/H \leq 12.5$, $0 \leq y/H \leq 24$, $0 \leq z/H \leq 1$) into cavity and intersection spaces and the vertical profiles averaged over the 12 cavity center (CC) points and those averaged over the 12 intersection center (IC) points (Fig. 1b) are compared in the NH and BH cases.

In the NH case, the vertical profiles of streamwise velocity over the CC and IC points have a logarithmic shape between $z/H = 1.5$ and 5. In both the NH and BH cases, below $z/H = 1.5$, the streamwise velocity over the IC points increases almost linearly with height and that over the CC points increases from negative to positive values with an inflection point at $z/H \sim 1$ (indicating a canyon vortex and a shear layer above the vortex). Compared with the NH case, flow just above the rooftop height ($z/H = 1$) is slightly accelerated and that above $z/H = 3$ is decelerated because of strengthened vertical mixing in the BH case. Bottom-heating effects are distinct in the

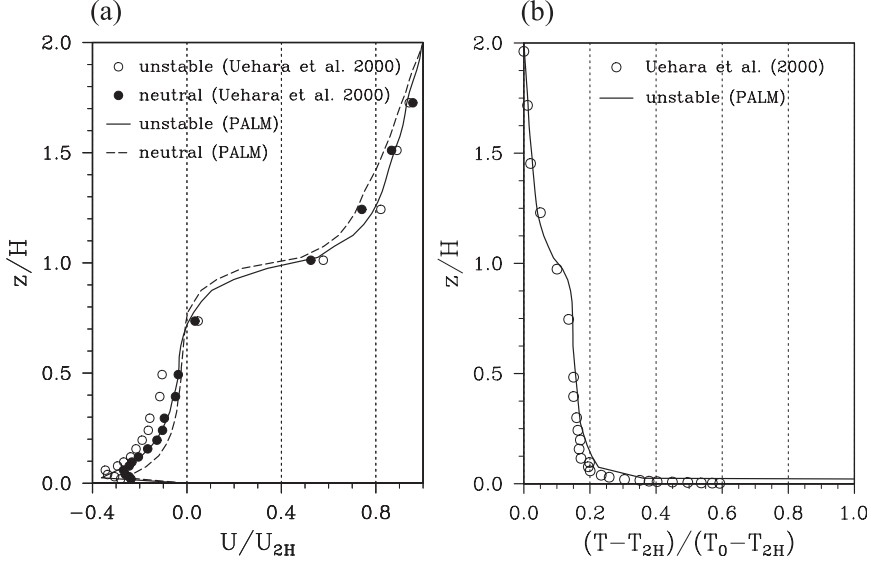


FIG. 2. Vertical profiles of (a) normalized streamwise velocity and (b) normalized temperature at the center of a street canyon in the present numerical simulation and the wind-tunnel experiment of Uehara et al. (2000); U_{2H} is the streamwise velocity at $z/H = 2$, T_{2H} is the temperature at $z/H = 2$, and T_0 is the temperature at $z/H = 0.002$ (very near the bottom surface).

vertical profiles of vertical turbulent momentum flux. Below $z/H = 2$, the magnitude of vertical turbulent momentum flux in the BH case is larger than that in the NH case over the CC and IC points. At the rooftop height, there are local peaks due to shear instability over the CC points in both the NH and BH cases. Below the rooftop height, the difference in the magnitude of vertical turbulent momentum flux between the CC points and IC points is more pronounced than the difference between the NH and BH cases (Fig. 3b).

In both the NH and BH cases, the vertical profile of $\sqrt{u'^2}$ averaged over the CC points has one peak at the rooftop height and that averaged over the IC points has two local peaks (one above the rooftop height and the other close to the bottom surface) (Fig. 3c). The vertical profiles of $\sqrt{w'^2}$ illustrate distinct thermal effects. Below $z/H = 2$ and above $z/H = 4$, $\sqrt{w'^2}$ in the BH case is larger than that in the NH case over the CC and IC points (Fig. 3d). While the difference below $z/H = 2$ is attributed to the increased shear and buoyancy production of turbulent kinetic energy in the BH case, the difference above $z/H = 4$ is attributed to the existence of large-scale updrafts and downdrafts above the bottom-heated building array. In the BH case, $\sqrt{w'^2}$ increases with height above $z/H = 4$ and reaches its maximum at $z/H \sim 15$ (a little higher than half the domain height). This is because large-scale vertical motions (comparable in size to the domain height) exist in the BH case, and they might affect flow structures in and above the building array.

b. Flow structures above a building array

Figure 4 shows the instantaneous fields of streamwise velocity and Q criterion at $y/H = 15$ and $t = 15\,480$ s in the NH case. The Q criterion is defined as the second invariant of the velocity gradient tensor (or half the difference between squared rotation rate and squared strain rate) and a positive value of Q criterion is widely used for detecting vortical flow structures (Dubief and Delcayre 2000). The instantaneous field of streamwise velocity in the x - z plane ($y/H = 15$) shows the large-scale structures of streamwise velocity, while that of Q criterion shows small-scale vortical structures induced by buildings or turbulent flow itself (Figs. 4a,b). In the streamwise velocity field, two kinds of characteristic interfaces appear in the regions where the vertical gradient of streamwise velocity is large. One is a local shear layer between the air in the cavity spaces and the air outside the cavities. The other is the interface between low- and high-speed air above the building array. Across the interface between low- and high-speed air, sinking of high-speed air and bursting of low-speed air occur continuously at a variety of scales. Sinking and bursting at the interface induce small-scale vortical structures (Fig. 4c), and they even squeeze or lift the interface itself when they grow in scale. In fact, the interface can be divided into two parts depending on the slope of the interface in the x - z plane. For example, part of the interface between $x/H = 6.5$ and 10.5 is upslope and

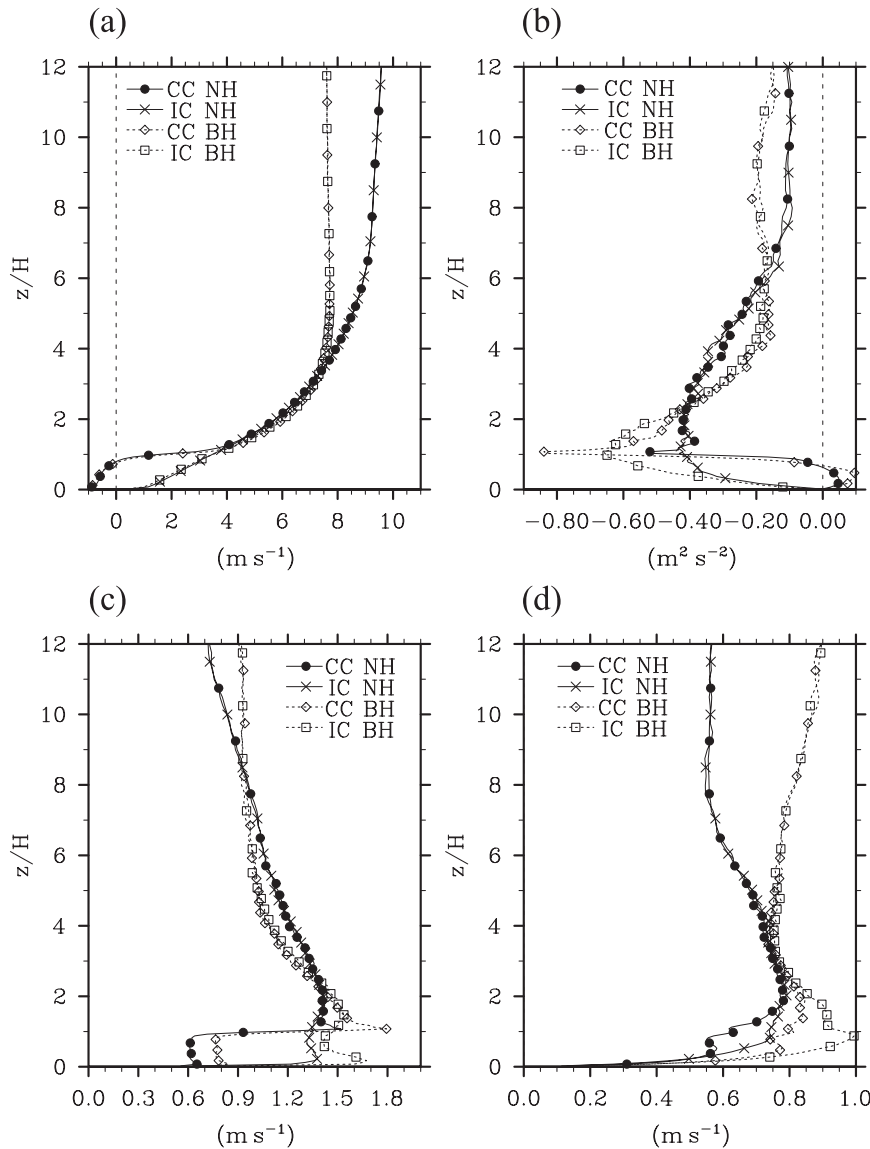


FIG. 3. Vertical profiles of 12 points-averaged (a) mean streamwise velocity, (b) vertical turbulent momentum flux, (c) RMS of streamwise velocity perturbation, and (d) RMS of vertical velocity perturbation. Sampling points are marked as hollow circles for CC and marked as filled squares for IC in Fig. 1b.

another part between $x/H = 12.5$ and 15 is downslope. While the sinking high-speed air squeezes low-speed air downstream across the upslope interface, the squeezed low-speed air and small-scale vortical structures in the squeezed low-speed air are burst upward, lifting the downslope interface and transporting momentum above the interface.

The turbulent motions related to the squeezing and lifting of the interface are repeated continuously in both the NH and BH cases, and this kind of turbulence coherent structure is similar to very large-scale motions

reported by Kim and Adrian (1999), Guala et al. (2006), and Hutchins and Marusic (2007). Although the generation mechanism of the large-scale coherent structures has not been clarified, it is clear that they play an important role in momentum transport (Guala et al. 2006) and affect velocity and scalar fields below them (Marusic et al. 2010; Inagaki et al. 2012). The interface that effectively describes the large-scale turbulent motions can be identified by plotting the vertical gradient of streamwise velocity or simply by plotting streamwise velocity (Figs. 4a,b). The latter method is selected in this

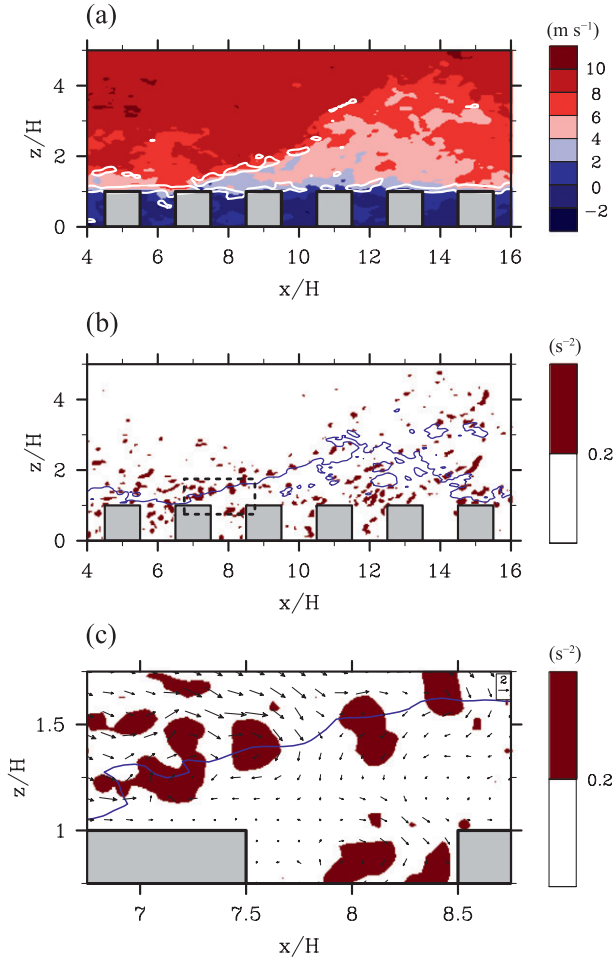


FIG. 4. Instantaneous fields of (a) streamwise velocity, (b) $\max(0, Q)$, and (c) $\max(0, Q)$ and velocity perturbation vector (u', w') in the x - z plane ($y/H = 15$) at $t = 15\,480$ s in the NH case. The small rectangle in dashed lines in (b) is the region of (c). Contours of the vertical gradient of streamwise velocity (1.3 s^{-1}) are added in (a), and contours of streamwise velocity magnitude (5.5 m s^{-1}) are added in (b) and (c).

study, and the contours of equal streamwise velocity magnitude (5.5 m s^{-1}) successfully depict turbulence coherent structures above the building array.

To investigate the detailed structures of large-scale turbulent motions above the building array and their role in momentum transport, two analysis heights are selected: $z/H = 1.2$ adjacent to the building tops and $z/H = 3$ in the inertial sublayer where flow is weakly or not affected by each individual roughness element. Figure 5 shows the fields of $\text{sgn}(w') \max(0, -u'w')$ at $t = 15\,480$ s in the NH case and the same fields at $t = 19\,080$ s in the BH case with equal streamwise velocity magnitude (5.5 m s^{-1}) being contoured. The $\max(0, -u'w')$ returns the magnitude of $u'w'$ only when $u'w'$ is negative (when momentum is transported downward), and $\text{sgn}(w')$

returns the sign of vertical velocity perturbation. Therefore, a positive value of $\text{sgn}(w') \max(0, -u'w')$ indicates an ejection event (a combination of negative u' and positive w') and a negative value indicates a sweep event (a combination of positive u' and negative w') following a typical definition used in the quadrant analysis (Raupach 1981).

In both the NH and BH cases, the contours of equal streamwise velocity magnitude (5.5 m s^{-1}) represent the interfaces of low- and high-speed air. In the y - z plane ($x/H = 16$) in the NH case, ejections on the lifted parts of the interface and sweeps on the sunken parts of the interface are distinct (Fig. 5a). The lifted and sunken parts of the interface are represented by dotted regions at $z/H = 3$ and hatched regions at $z/H = 1.2$, respectively (Figs. 5b,c). At $z/H = 3$ and $t = 15\,480$ s, the low-speed air lifted by successive ejections forms streamwise-elongated low-speed regions (at $y/H \sim 5$) and a group of low-speed streaks (at $y/H \sim 17$) (Fig. 5b). Usually two or three, and sometimes one row of low-speed flow structures appear and the spanwise scales of the rows are sensitive to the upper flow above $z/H = 3$. Actually, large-scale secondary circular flow covers the whole x - y plane above $z/H \sim 7$ (not shown) and it affects the relative magnitude of turbulent motions below it. Low-speed upper flow induces stronger ejections and wider low-speed regions at $y/H \sim 5$ relative to the flow structures at $y/H \sim 17$. At $z/H = 1.2$, the high-speed air sunk by sweeps forms high-speed streaks and their spanwise scales are smaller than those at $z/H = 3$ because of the influence of buildings (Fig. 5c). Some of the high-speed streaks penetrate into cavity and intersection spaces and affect flow therein. Above the building array, momentum is transported always downward by ejections and sweeps. Strong ejections and weaker sweeps transport momentum downward at $z/H = 3$ (Fig. 5b), while strong sweeps and weaker ejections transport momentum downward at $z/H = 1.2$ (Fig. 5c). Although the area occupied by ejections is smaller than the area occupied by sweeps at $z/H = 3$, the magnitude of vertical turbulent momentum flux by ejections ($\overline{u'_- w'_+}$) is larger than that by sweeps ($\overline{u'_+ w'_-}$) in the NH case, indicating the effectiveness of ejections in momentum transport at $z/H = 3$ (Table 1). By contrast, the vertical turbulent momentum flux by sweeps and that by ejections are similar in magnitude at $z/H = 1.2$ (Table 1).

At $z/H = 3$ and $t = 19\,080$ s in the BH case, there exist a streamwise-elongated low-speed region at $y/H \sim 1$ that expands vertically up to $z/H = 5$ and several plume-shaped low-speed flow structures between $y/H = 6$ and 20 (Figs. 5d,e). In the BH case, large-scale secondary circular flow (stronger than that in the NH case) dominates the whole model domain with updrafts intensified

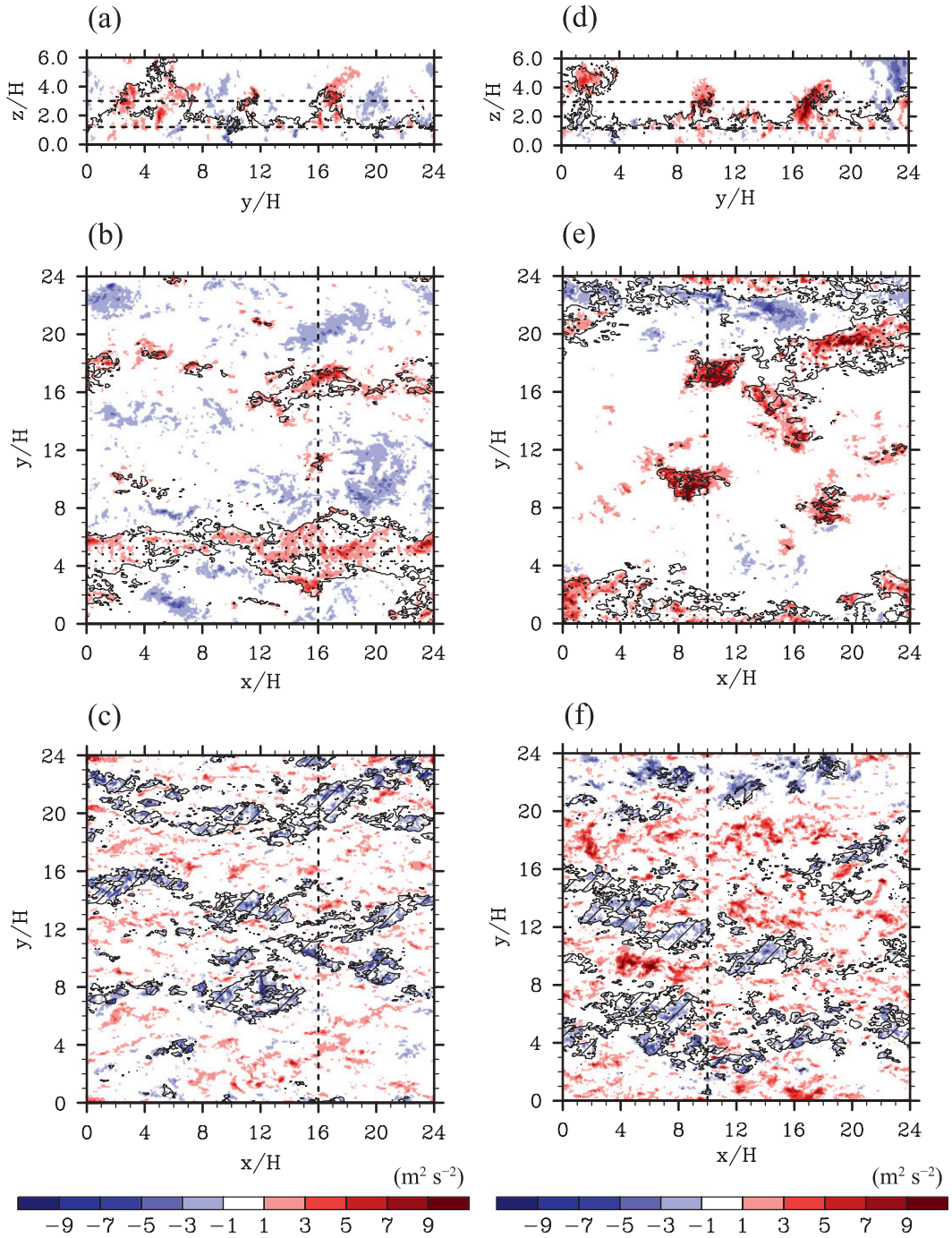


FIG. 5. Instantaneous fields of $\text{sgn}(w') \max(0, -u'w')$ and the contours of equal streamwise velocity (5.5 m s^{-1}) at $t = 15\,480$ s in the (a) $y-z$ plane ($x/H = 16$), (b) $x-y$ plane ($z/H = 3$), and (c) $x-y$ plane ($z/H = 1.2$) in the NH case and the same fields at $t = 19\,080$ s in the (d) $y-z$ plane ($x/H = 10$), (e) $x-y$ plane ($z/H = 3$), and (f) $x-y$ plane ($z/H = 1.2$) in the BH case.

by bottom heating. In fact, this study mainly focuses on flow structures in the surface layer. Thus, the vertical scale of the simulated large secondary circular flow in the BH case might be limited by the model domain height

and it could be smaller than the vertical scale of flow in a typical convective boundary layer (approximately inversion height). Although the thermal secondary circular flow is not fully simulated, characteristic features

TABLE 1. Areas occupied by low-speed regions (LSR) and high-speed regions (HSR) at $z/H = 3$ and time- and area-averaged streamwise velocity, vertical velocity, vertical turbulent momentum flux, ratio of vertical turbulent momentum flux by ejections ($\langle u'_- w'_+ \rangle$) to that by sweeps ($\langle u'_+ w'_- \rangle$), and $\max(0, Q)$ on the total horizontal domain, LSR, and HSR at $z/H = 3, 1.2, 1$, and 0.5 in the NH and BH cases. Overbars and angle brackets represent time-average and area-average, respectively.

Cases Region	NH			BH		
	Total	LSR	HSR	Total	LSR	HSR
Area (%)	100	30.8	33.3	100	23.9	35.8
$\langle u \rangle_{3H}$ (m s ⁻¹)	7.05	5.33	8.62	7.13	4.84	8.49
$\langle w \rangle_{3H}$ (m s ⁻¹)	0.00	0.35	-0.32	0.00	0.71	-0.33
$\langle u'w' \rangle_{3H}$ (m ² s ⁻²)	-0.37	-0.60	-0.47	-0.32	-0.83	-0.18
$\langle \langle u'_- w'_+ \rangle / \langle u'_+ w'_- \rangle \rangle_{3H}$	1.11	92.14	0.01	1.47	16.92	0.04
$\langle \max(0, Q) \rangle_{3H}$ (s ⁻²)	0.03	0.04	0.03	0.03	0.06	0.02
$\langle u \rangle_{1.2H}$ (m s ⁻¹)	3.80	3.20	4.30	4.08	2.88	4.67
$\langle w \rangle_{1.2H}$ (m s ⁻¹)	0.00	0.06	-0.05	0.00	0.16	-0.06
$\langle u'w' \rangle_{1.2H}$ (m ² s ⁻²)	-0.42	-0.36	-0.48	-0.60	-0.58	-0.61
$\langle \langle u'_- w'_+ \rangle / \langle u'_+ w'_- \rangle \rangle_{1.2H}$	0.98	2.27	0.55	1.07	2.03	0.82
$\langle \max(0, Q) \rangle_{1.2H}$ (s ⁻²)	0.08	0.07	0.09	0.10	0.09	0.11
$\langle u \rangle_H$ (m s ⁻¹)	2.58	2.16	2.92	2.70	1.85	3.11
$\langle w \rangle_H$ (m s ⁻¹)	0.00	0.04	-0.05	0.00	0.15	-0.06
$\langle u'w' \rangle_H$ (m ² s ⁻²)	-0.40	-0.35	-0.45	-0.63	-0.58	-0.63
$\langle \langle u'_- w'_+ \rangle / \langle u'_+ w'_- \rangle \rangle_H$	0.80	1.55	0.50	0.85	1.39	0.71
$\langle \max(0, Q) \rangle_H$ (s ⁻²)	0.09	0.07	0.10	0.12	0.10	0.13
$\langle u \rangle_{0.5H}$ (m s ⁻¹)	1.32	1.05	1.53	1.26	0.66	1.58
$\langle w \rangle_{0.5H}$ (m s ⁻¹)	0.00	0.02	-0.02	0.00	0.09	-0.03
$\langle u'w' \rangle_{0.5H}$ (m ² s ⁻²)	-0.15	-0.14	-0.16	-0.22	-0.21	-0.21
$\langle \langle u'_- w'_+ \rangle / \langle u'_+ w'_- \rangle \rangle_{0.5H}$	0.88	1.48	0.62	0.94	1.28	0.82
$\langle \max(0, Q) \rangle_{0.5H}$ (s ⁻²)	0.06	0.05	0.07	0.09	0.08	0.10

such as streamwise-elongated flow structures are well simulated. Above $z/H \simeq 2$, the strengthened secondary circular flow induces low-speed regions ($23 < y/H < 24$ and $0 < y/H < 3$) and wide high-speed regions ($4 < y/H < 20$) and the low- and high-speed regions are stable enough to be detected in the time-averaged fields. At $z/H = 3$, successive ejections occur in the existing low-speed regions, while ejections in the high-speed regions occur occasionally forming the plume-shaped low-speed flow structures (Fig. 5e). At $z/H = 1.2$ in the BH case, ejections that are stronger and larger than those in the NH case appear with sweeps, and these ejections and sweeps together play an important role in momentum transport (Fig. 5f).

Compared with the NH case, it seems that stronger ejections appear in shrinking low-speed regions in the x - y plane ($z/H = 3$) in the BH case (Fig. 5e). This feature is quantified by comparing areas occupied by newly defined low-speed regions ($u < \bar{u} - \sqrt{\bar{u}'^2}$) and high-speed regions ($u > \bar{u} + \sqrt{\bar{u}'^2}$) at $z/H = 3$ and by comparing vertical turbulent momentum fluxes averaged

over the low- and high-speed regions for each case (Table 1). In the NH case, the area of low-speed regions is similar to that of high-speed regions and the magnitude of the averaged vertical turbulent momentum flux in the low-speed regions is larger than that in the high-speed regions. In the BH case, however, the area of low-speed regions is smaller than that of high-speed regions by 11.9% and the magnitude of the averaged vertical turbulent momentum flux in the low-speed regions is 4.6 times larger than that in the high-speed regions. This indicates that more momentum is transported through shrunken low-speed regions over the bottom-heated building array than in the NH case. Furthermore, the magnitude of the averaged vertical velocity in the low-speed regions increases by more than 2 times and that of the averaged streamwise velocity in the low-speed regions decreases significantly relative to the NH case (Table 1), highlighting the importance of low-speed flow structures in the BH case.

Figure 6 shows the fields of joint probability density of u' and w' and $u'w'$ multiplied by the joint probability density at $z/H = 3$ in the NH and BH cases. The joint probability density of u' and w' is calculated using the expression $f_{u',w'}(a_i, a_j) = P(a_i - 0.5\Delta a < u' \leq a_i + 0.5\Delta a, a_j - 0.5\Delta a < w' \leq a_j + 0.5\Delta a)$. The number in each direction N and spacing Δa of bins used to calculate the joint probability distribution are 50 and 0.2, respectively, and the sum of all joint probability densities $\sum_{i=1}^N \sum_{j=1}^N f_{u',w'}(a_i, a_j)$ is 1. The joint probability density and $u'w'$ multiplied by the joint probability density can easily illustrate the frequency of turbulent events (u', w') and their contribution to vertical turbulent momentum flux, respectively. In the NH case, ejections and sweeps are comparable in frequency. However, strong ejections ($u'w' < -2.5$ m² s⁻²) occur a little more frequently than strong sweeps, resulting in more contribution of ejections to vertical turbulent momentum flux. In the BH case, weak turbulent events (close to the origin in the u' - w' plane) occur more frequently than in the NH case and strong turbulent events are concentrated in the second quadrant (ejection). The thermally affected joint probability density distribution in the BH case induces more contribution to vertical turbulent momentum flux by ejections (Fig. 6d). As the height approaches $z/H = 1$, the joint probability density distribution becomes similar to that at $z/H = 3$ in the NH case (Fig. 6a) and the difference between the NH and BH cases becomes smaller (not shown).

To examine the essential flow structures of large-scale turbulent motions such as low-speed streaks, conditionally averaged fields of streamwise velocity perturbation and velocity vector are plotted in Fig. 7. Conditional averages are obtained using the following steps. First, local

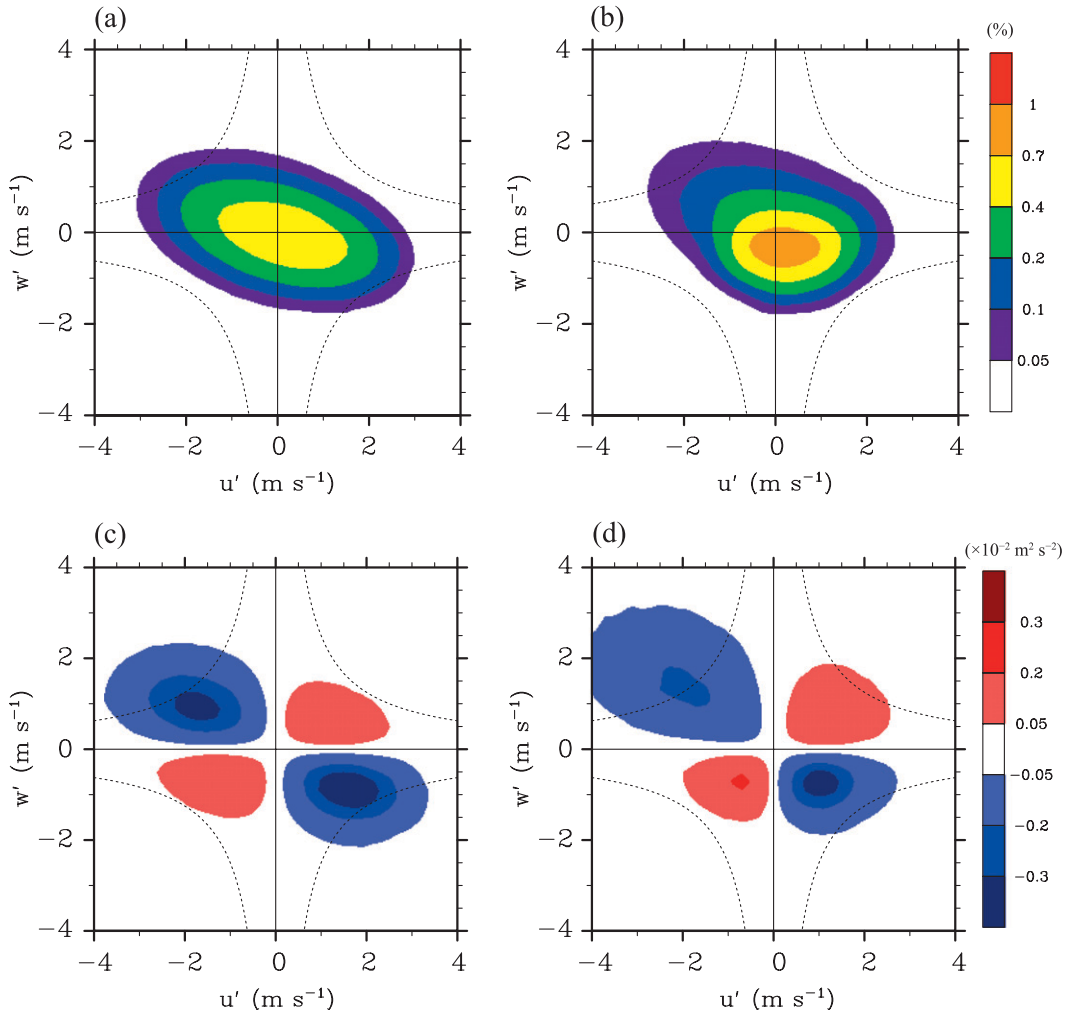


FIG. 6. Fields of the joint probability density of u' and w' in the (a) NH and (b) BH cases and $u'w'$ multiplied by the joint probability density in the (c) NH and (d) BH cases at $z/H = 3$. Dashed lines of equal $|u'w'|$ ($2.5 \text{ m}^2 \text{ s}^{-2}$) are added.

minimum points of $u'w'$ in the regions satisfying a certain criterion (e.g., $u'w' < -2.5 \text{ m}^2 \text{ s}^{-2}$) are identified in the x - y plane ($z/H = 3$). Then, the three-dimensional data of a target variable are transformed to a coordinate (x' , y' , z) centered on each minimum point and the transformed data are collected. The identifying and collecting steps are repeated for successive instants. Finally, the collected three-dimensional data are averaged. In this study, we apply the criterion based on the magnitude of vertical turbulent momentum flux to extract the essential flow structures that are important for momentum transport. The criterion can be changed depending on the objective of conditional averaging. For all the velocity vector plots, conditionally averaged u' is used instead of u to emphasize the relative motion of coherent structures with respect to the mean flow.

The conditionally averaged fields show the elliptical structures of negative streamwise velocity perturbation with low pressure perturbation (represented by the contours in Fig. 7). In the NH case, the obtained elliptical structure is composed of low-speed and upward turbulent motions, indicating the dominance of ejections above the building array. The contours of low pressure perturbation in Fig. 7 represent vortices (mostly streamwise vortices) around low-speed flow structures in the instantaneous flow fields (not shown), and their shape in the conditionally averaged fields resembles hairpin vortices (Adrian et al. 2000; Coceal et al. 2007). Although a positive Q criterion is known to be more accurate for detecting small-scale vortical structures than low pressure perturbation (Dubief and Delcayre 2000), low pressure perturbation is used for plotting vortices because Q criterion

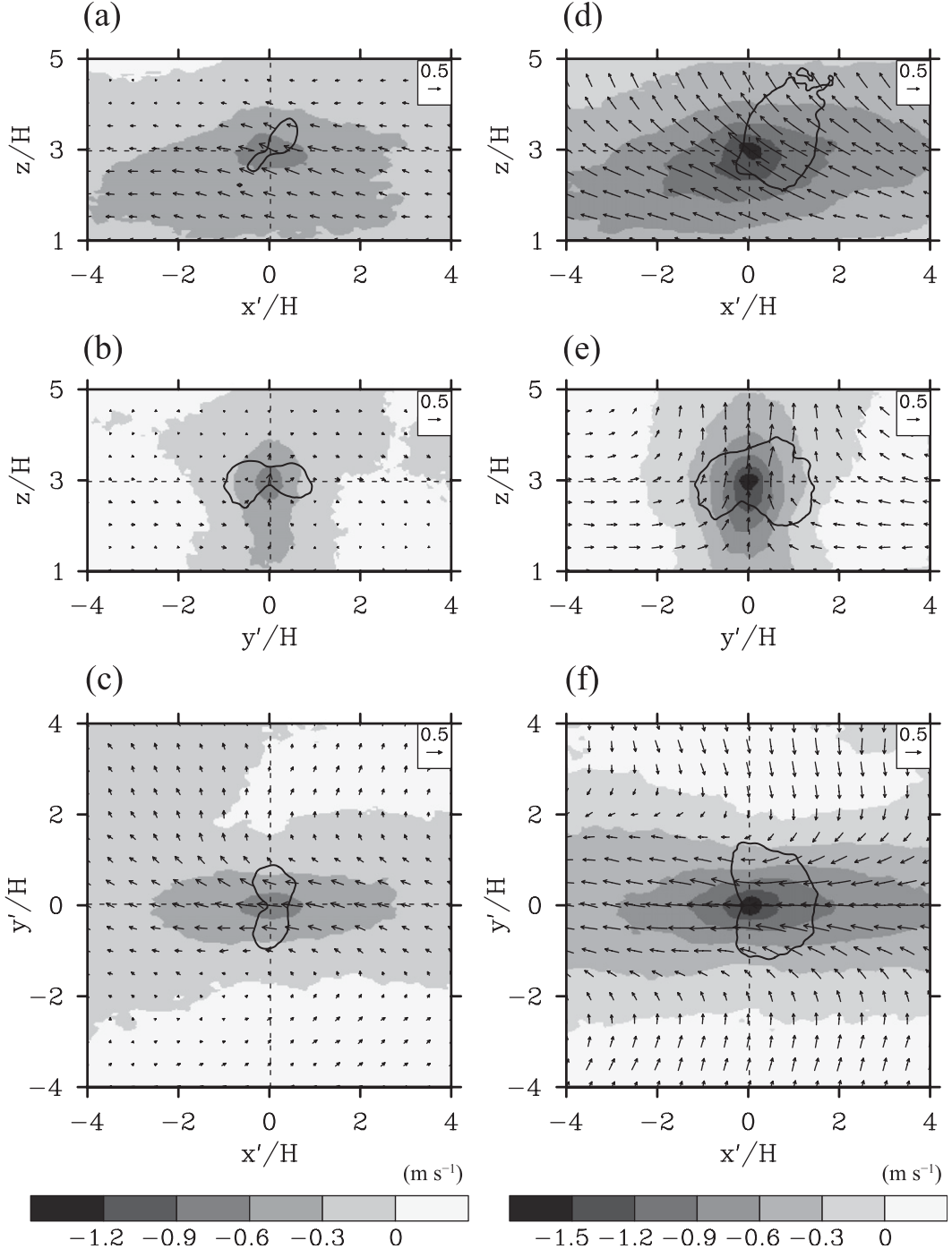
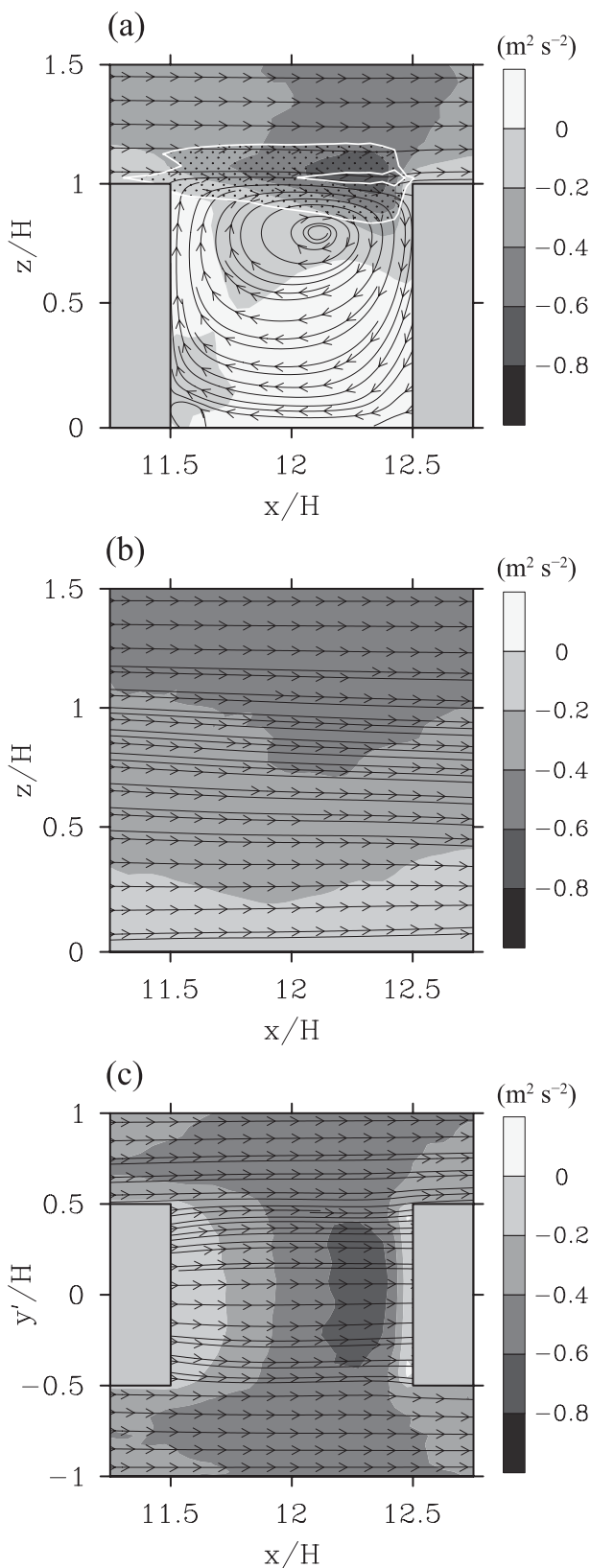


FIG. 7. Conditionally averaged u' and velocity vector fields in the (a) $x'-z$ plane ($y'/H = 0$), (b) $y'-z$ plane ($x'/H = 0$), and (c) $x'-y'$ plane ($z/H = 3$) in the NH case and the same conditionally averaged fields in the (d) $x'-z$ plane ($y'/H = 0$), (e) $y'-z$ plane ($x'/H = 0$), and (f) $x'-y'$ plane ($z/H = 3$) in the BH case. Conditionally averaged u' instead of u is used for plotting velocity vector fields, and the contours of equal conditionally averaged pressure perturbation (-1 Pa in the NH case and -1.5 Pa in the BH case) are added.



cannot illustrate vertical structures larger than the building height. Actually, streamwise vortices frequently appear in and above the building array in the instantaneous pressure fields (not shown) and they play an important role in inducing strong ejections. The newly ejected low-speed air (by the streamwise vortices) forms low-speed streaks next to the existing low-speed flow structures, resulting in the horizontal meandering of low-speed regions in the NH case (Fig. 5b). However, the interaction of the streamwise vortices with turbulent motions in and above the building array is still not completely understood.

In the BH case, the magnitudes of velocity perturbation in the x and z directions increase and y direction motions toward the center line ($y'/H = 0$) strengthen (Figs. 7d–f). The shape of conditionally averaged low pressure perturbation in the BH case is different from that in the NH case. The head part of the hairpin vortexlike structure is expanded vertically, possibly because of ascending thermal plumes. In the instantaneous pressure fields in the BH case, more vertically slanted vortices are observed (not shown) and they are closely related to the plume-shaped low-speed flow structures (Fig. 5e). Relative to the NH case, bottom heating strengthens low-speed flow structures much above the building array (Fig. 7). The mean flow above $z/H = 3$ is weaker in the BH case than in the NH case (Fig. 3a).

c. Flow structures in a building array

Figure 8 shows vertical turbulent momentum flux ($\bar{u}'\bar{w}'$) fields spanwise averaged over the 12 x - z cross sections containing the CC points, those containing the IC points, and the 12 CC-centered subregions at the rooftop height in the NH case. In the NH case, a shear layer develops around the tops of cavity spaces and the shear layer can be identified by the vertical gradient of shear production (Salizzoni et al. 2011). In the x - z cross sections containing the CC points, the vertical gradient of shear production is calculated and contours of absolute value 0.06 m s^{-3} are plotted in Fig. 8a. Going downstream from the upper corner of upwind buildings, the shear layer develops and its thickness reaches a

FIG. 8. Vertical turbulent momentum flux ($\bar{u}'\bar{w}'$) fields spanwise averaged over (a) the 12 x - z cross sections containing the CC points, (b) those containing the IC points, and (c) the 12 CC points-centered subregions at $z/H = 1$ (Fig. 1b) in the NH case. Contours of equal absolute value of the vertical gradient of shear production of turbulent kinetic energy (0.06 m s^{-3}) are added in (a). The dotted region in (a) indicates the region where the absolute value of the vertical gradient of shear production of turbulent kinetic energy is $> 0.06 \text{ m s}^{-3}$. Streamlines are also plotted.

maximum in front of downwind buildings. Near the upper corner of downwind buildings, the shear layer tends to develop downward following the primary vortex in the cavity spaces. In and around the shear layer, turbulent eddies generated by the upwind buildings or by flow structures passing over the building array grow and strengthen as they move downstream. Consequently, the maximum $\overline{u'w'}$ appears near the upper corner of downwind buildings (Figs. 8a,c). In the x - z cross sections containing the IC points, the shear layer is not detected and the magnitude of $\overline{u'w'}$ increases with height (Fig. 8b). This indicates that turbulent flow in the intersection spaces is closely related to the upper turbulent flow structures such as high-speed streaks.

Figure 9 shows streamwise velocity perturbation and velocity vector fields conditionally averaged over the tops of cavity spaces and those over the tops of intersection spaces in the NH case. As compared with the conditionally averaged fields at $z/H = 3$, sweeps are dominant at the rooftop height and their horizontal size is much smaller than that at $z/H = 3$ in the NH case. At the tops of cavities, the structure of sweeps is circular in the x' - y' plane and elliptical in the x' - z and y' - z planes, indicating a flat-disk shape in a three-dimensional space. At the tops of intersections, however, the structure of sweeps is streamwise elongated in the x' - y' plane and the magnitude of streamwise velocity perturbation decreases compared with that at the tops of cavities. Sweep-dominant structures have also been found over plant canopies (Fitzmaurice et al. 2004; Watanabe 2004) although the detailed shape of the structures is different because of the difference in the criteria used for conditional averaging. As shown in Fig. 9, velocity fluctuations (represented by low pressure perturbations) above the cavity spaces and those in and above the intersection spaces tend to appear upstream of the point $(x', y', z) = (0, 0, H)$ because the structures induce sweeps on their downstream sides. In the cavity spaces, vortex flow structures (also represented by low pressure perturbations) appear and they are connected to the velocity fluctuations passing over the cavity spaces (Fig. 9a). This kind of connected structures might lead to the strong vertical turbulent momentum flux in front of downwind buildings (Figs. 8a,c). As in the NH case, same turbulence coherent structures with a flat-disk shape at the tops of cavity spaces and a streamwise-elongated shape at the tops of intersection spaces appear in the BH case because of the dominant influence of buildings at the rooftop height (not shown).

Figure 10 shows vertical turbulent momentum flux ($\overline{u'w'}$) field spanwise averaged over the 12 x - z cross sections containing the CC points and correlation coefficient field of temperature and $u'w'$ averaged over the

same cross sections in the BH case. In the x - z cross sections containing the CC points, bottom heating induces stronger vertical turbulent momentum flux and the shear layer becomes thicker (Fig. 10a) because of the increase of shear production there relative to the NH case (Fig. 8a). As shown in Fig. 10b, the vertical turbulent momentum flux and temperature are well correlated in and around the shear layer, but the signs of correlation coefficients are opposite depending on the height. The correlation coefficient is negative in the upper part of the shear layer and positive in the lower part of the shear layer. Judging from the fact that the common turbulent events in the upper and lower parts of the shear layer are the bursting of cavity air (high-temperature perturbation) and the entrainment of ambient air (low-temperature perturbation), the negative and positive correlation coefficients are closely related to ejections in the upper part of the shear layer and sweeps in the lower part of the shear layer. In fact, both ejections and sweeps in the BH case have larger magnitudes than those in the NH case, resulting in stronger vertical turbulent momentum flux in the shear layer (Fig. 10a).

Figure 11 shows vertical turbulent momentum flux ($\overline{u'w'}$) and spanwise turbulent momentum flux ($\overline{u'v'}$) fields spanwise averaged over the 12 CC-centered subregions at $z/H = 0.5$ in the NH case. The magnitude of vertical turbulent momentum flux is larger in the intersection spaces than in the cavity spaces because the high-speed upper air occasionally penetrates into the intersection spaces, transporting momentum downward. In the cavity spaces, however, the vortical flow structures such as a primary vortex in the x - z plane (Fig. 8a) and a double-eddy circulation in the x - y plane at $z/H = 0.5$ (Fig. 11) interrupt the deep penetration of the high-speed upper air, resulting in weakly downward or upward turbulent transport of momentum. Spanwise turbulent motions appear around the boundaries between the cavity and intersection spaces, leading to strong spanwise turbulent momentum flux there (Fig. 11b). In the BH case, similar vertical and spanwise turbulent momentum flux fields appear at $z/H = 0.5$, indicating the momentum transport from above the rooftop height into the cavity spaces.

Streamwise velocity perturbation and velocity vector fields with the contours of equal vertical velocity (-0.23 m s^{-1}), all conditionally averaged at $z/H = 0.5$ in the intersection spaces, are shown in Fig. 12. In both the NH and BH cases, the structure that is composed of positive streamwise velocity perturbation and downdraft ($w < -0.23 \text{ m s}^{-1}$) appears with spanwise diverging flow. This again indicates that the high-speed upper air comes into the intersection spaces and induces spanwise motions

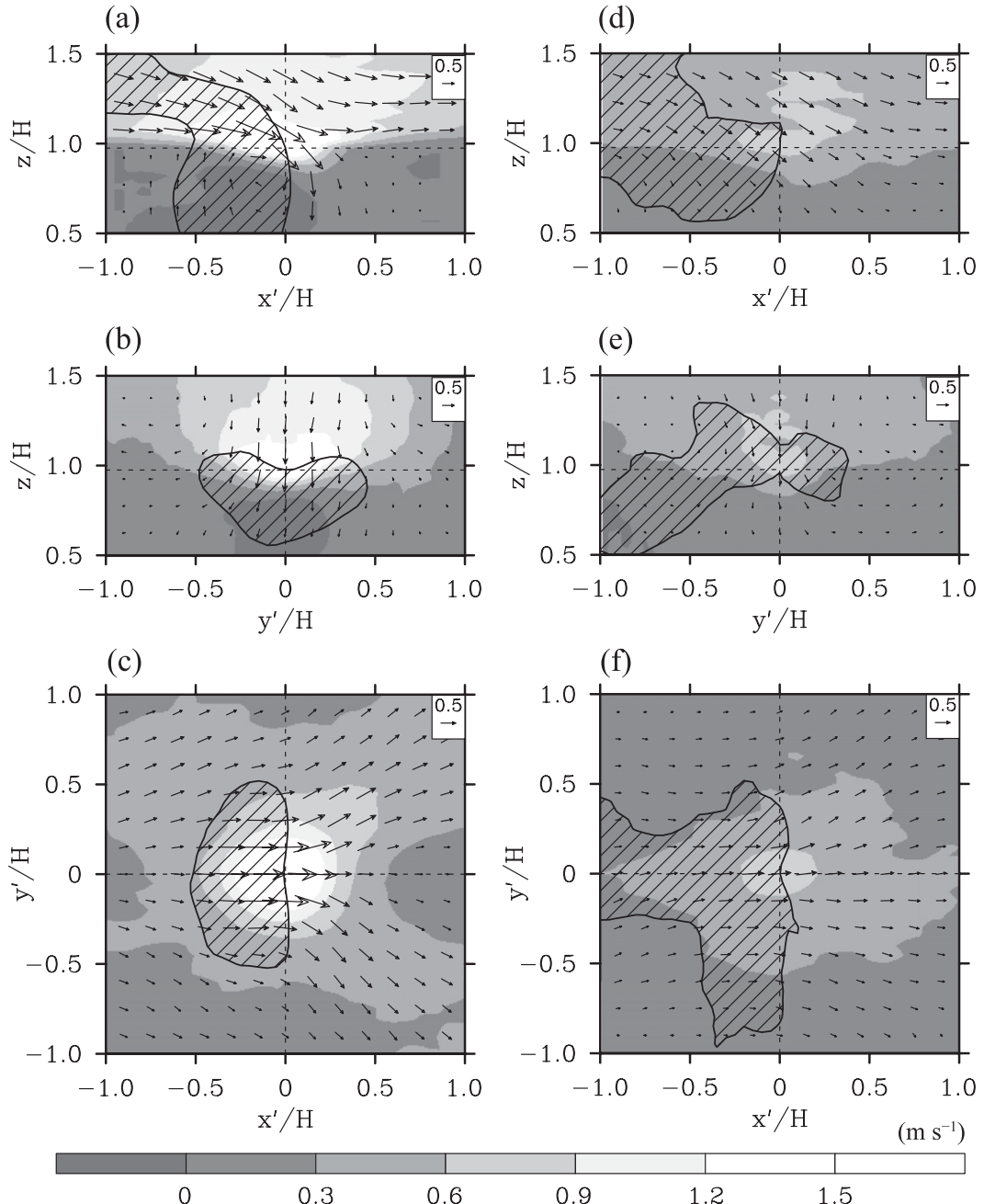


FIG. 9. The u' and velocity vector fields in the (a) x' - z plane ($y'/H = 0$), (b) y' - z plane ($x'/H = 0$), and (c) x' - y' plane ($z/H = 1$) conditionally averaged at the tops of the cavity spaces, and the same fields in the (d) x' - z plane ($y'/H = 0$), (e) y' - z plane ($x'/H = 0$), and (f) x' - y' plane ($z/H = 1$) conditionally averaged at the tops of the intersection spaces in the NH case. Conditionally averaged u' instead of u is used for plotting velocity vector fields, and the contours of equal conditionally averaged pressure perturbation (-0.95 Pa) are added. The hatched areas indicate the regions where conditionally averaged pressure perturbation is $<-0.95 \text{ Pa}$.

heading for nearby cavity spaces. The structure of positive streamwise velocity perturbation in the NH case has a more elongated shape and larger magnitude than that in the BH case. As indicated by the contours around $(x', y') = (0.5, -1.0)$ or $(0.5, 1.0)$ (corresponding to the spaces

in front of downwind buildings) in Fig. 12, sweeps tend to appear in the intersection spaces with downdrafts in the nearby cavity spaces in both cases. This is because overlying high-speed streaks (larger than the building height) induce sweeps in the intersection spaces and the streaks

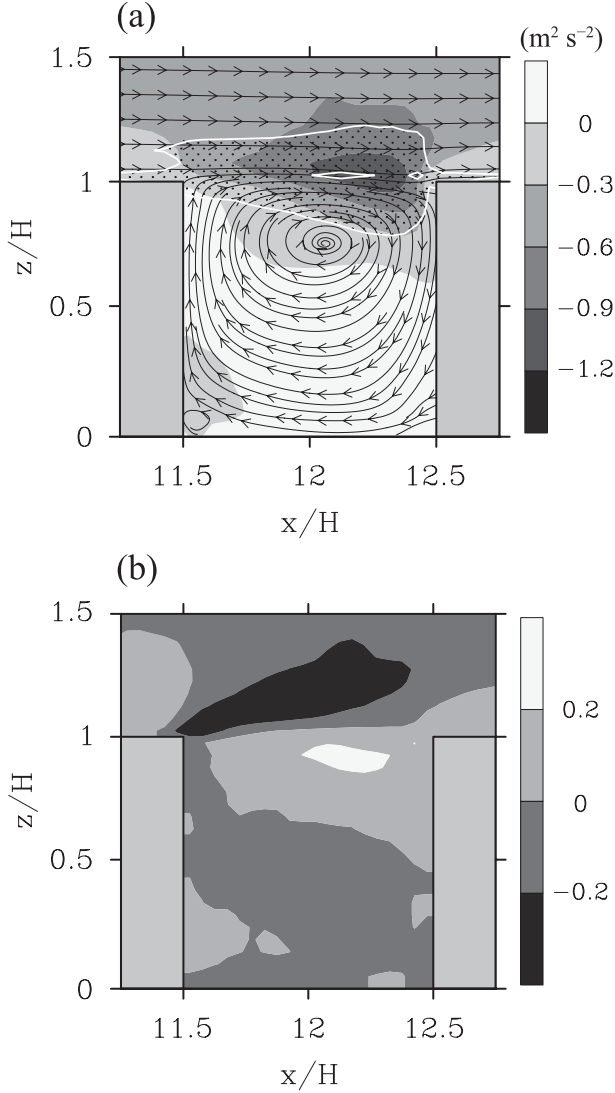


FIG. 10. Fields of (a) vertical turbulent momentum flux ($\langle \bar{u}'w' \rangle$) spanwise averaged over the $12x-z$ cross sections containing the CC points and (b) correlation coefficient of temperature and $u'w'$ averaged over the same cross sections in the BH case. Streamlines and contours of equal absolute value of the vertical gradient of shear production of turbulent kinetic energy (0.06 m s^{-3}) are added in (a). The dotted region in (a) indicates the region where the absolute value of the vertical gradient of shear production of turbulent kinetic energy is $> 0.06 \text{ m s}^{-3}$.

simultaneously induce downdrafts in the nearby cavity spaces.

As shown in Table 1, the magnitude of area-averaged vertical turbulent momentum flux at $z/H = 1$ and 1.2 below the high-speed regions (defined at $z/H = 3$) is larger than that below the low-speed regions in both the NH and BH cases, and the signs of area-averaged vertical velocity are negative and positive below the high- and low-speed regions, respectively. Moreover, the time- and

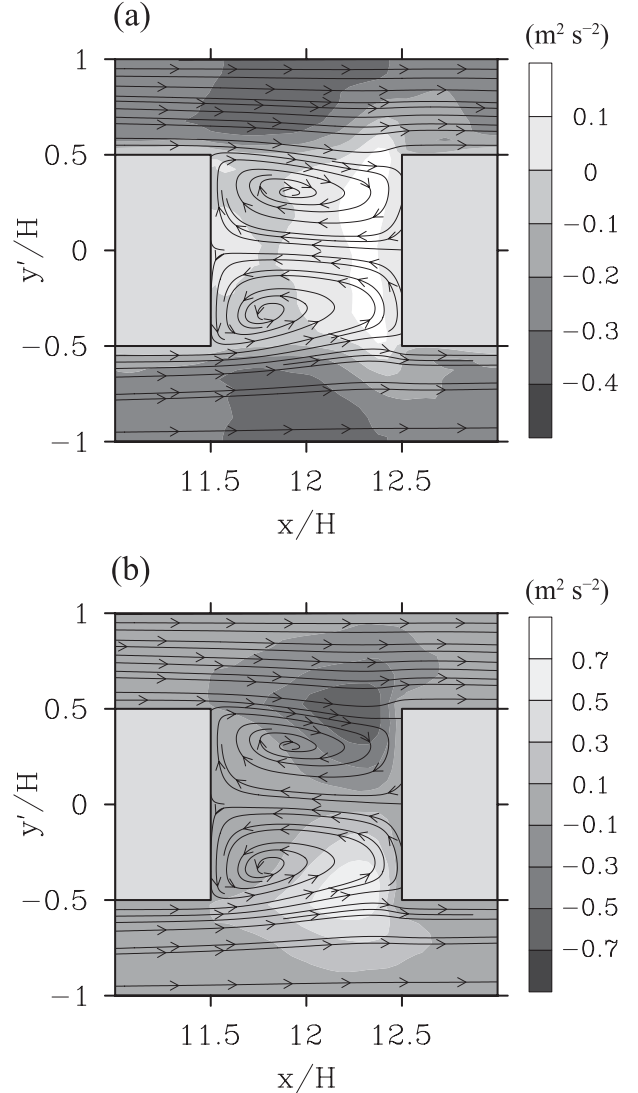


FIG. 11. Fields of (a) vertical turbulent momentum flux ($\langle \bar{u}'w' \rangle$) and (b) spanwise turbulent momentum flux ($\langle \bar{u}'v' \rangle$) spanwise averaged over the 12 CC-centered subregions at $z/H = 0.5$ in the NH case. Streamlines are also plotted.

area-averaged $\max(0, Q)$ at $z/H = 1$ and 1.2 below the high-speed regions is larger than that below the low-speed regions in both the NH and BH cases. The averaged value of $\max(0, Q)$ returns the averaged intensity of small-scale vortical structures, and it is closely related to the number of small-scale vortical structures. Thus, the larger magnitude of time- and area-averaged $\max(0, Q)$ below the high-speed regions indicates that more small-scale vortical structures exist below the high-speed regions than below the low-speed regions. This implies that high-speed streaks passing over the building array induce downward-tilted flow impinging on buildings and more small-scale vortical structures appear around the buildings,

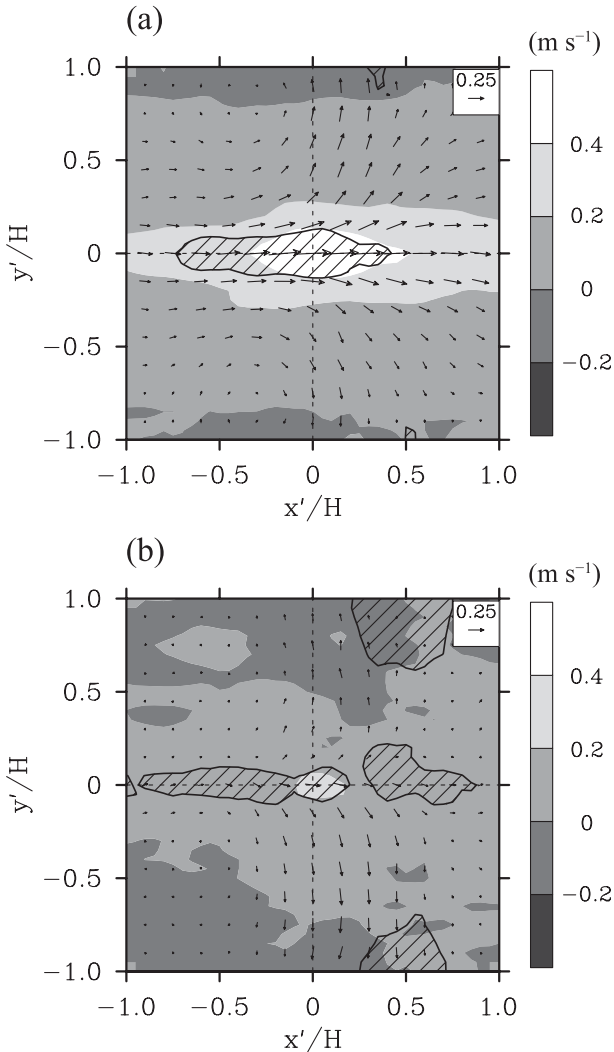


FIG. 12. Streamwise velocity perturbation and velocity vector fields in the x' - y' plane ($z/H = 0.5$) conditionally averaged at $z/H = 0.5$ in the intersection spaces in the (a) NH and (b) BH cases. Conditionally averaged u' instead of u is used for plotting velocity vector fields and the contours of equal conditionally averaged vertical velocity (-0.23 m s^{-1}) are added. The hatched areas indicate the regions where conditionally averaged downward vertical velocity is higher than 0.23 m s^{-1} .

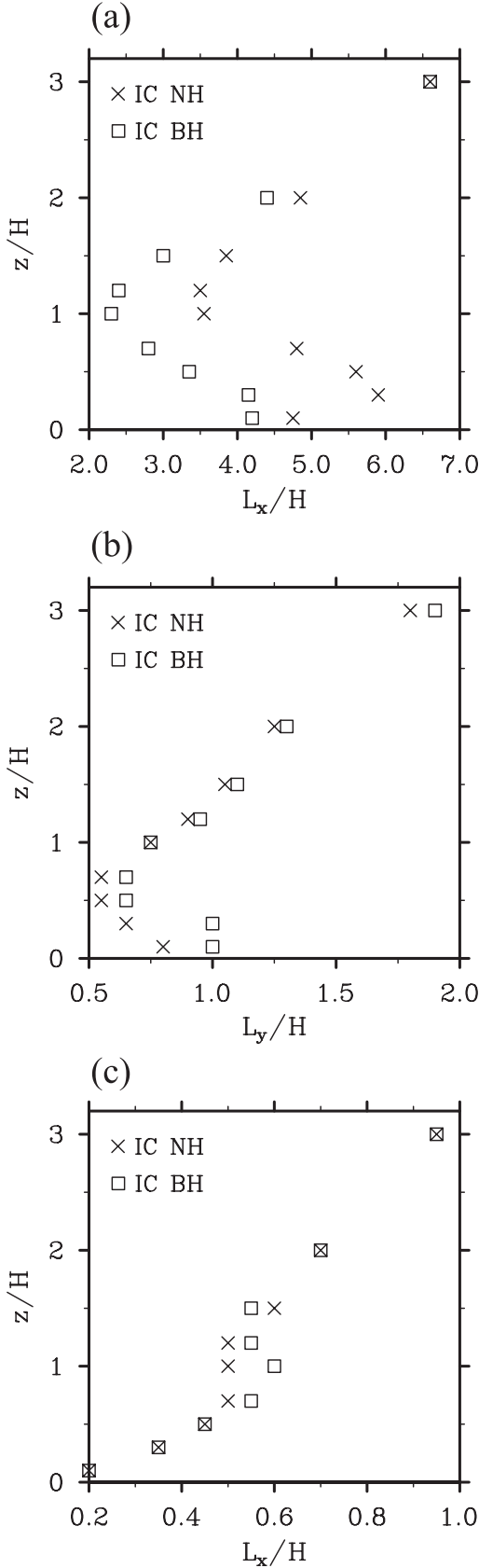
leading to the stronger vertical turbulent momentum flux below the high-speed regions. On the contrary, low-speed streaks seem to induce updrafts and fewer small-scale structures below them in the building array. These findings are consistent with the conceptual model of turbulent flow over a flat plate (Marusic et al. 2010).

In contrast to the intersection spaces, the magnitude of vertical turbulent momentum flux in the cavity spaces is quite small. Therefore, conditionally averaged fields using the criterion based on turbulent kinetic energy are investigated. The conditionally averaged fields show

a typical canyon vortex in the x' - z plane and a double-eddy circulation in the x' - y' plane at $z/H = 0.5$ (not shown), commonly observed in time-averaged velocity vector fields in a building array (Santiago et al. 2007).

Figure 13 shows the vertical profiles of 12 points-averaged streamwise length scale of streamwise velocity, spanwise length scale of spanwise velocity, and streamwise length scale of vertical velocity over the IC points in the NH and BH cases. All length scales are obtained by calculating maximum streamwise (or spanwise) distance between the points where the correlation coefficient of each variable is 0.5. The streamwise length scale of streamwise velocity increases with height above the rooftop height in both cases. Below $z/H = 3$, the streamwise length scale of streamwise velocity in the BH case is smaller than that in the NH case, indicating that bottom heating obstructs the passage of high-speed streaks. This corresponds to the shortened high-speed streaks in the BH case (Fig. 12b). The spanwise length scale of spanwise velocity below the rooftop height in the BH case is larger than that in the NH case. This indicates that bottom heating induces stronger spanwise motions in the building array. The streamwise (also spanwise) length scale of vertical velocity does not show any noticeable difference between the NH and BH cases.

As shown in Fig. 12, high-speed streaks from above the building array induce spanwise flow in the building array. Actually, the spanwise range affected by the overlying turbulent flow structures is larger than the building height and sometimes equal to the horizontal domain size depending on the stability. Figure 14 shows time-averaged spanwise velocity fields at $z/H = 0.1$ with the contours of equal streamwise velocity magnitude at $z/H = 3$ and those at $z/H = 1.2$ in the NH and BH cases. Dotted regions indicate the low-speed streaks or low-speed regions in the time-averaged streamwise velocity fields at $z/H = 3$, and hatched regions indicate the high-speed streaks in the time-averaged streamwise velocity fields at $z/H = 1.2$. In the NH case, high-speed regions ($\bar{u} > 4.4 \text{ m s}^{-1}$ at $z/H = 1.2$) and one low-speed region ($\bar{u} < 6.0 \text{ m s}^{-1}$ at $z/H = 3$) above the building array induce spanwise diverging and converging flow at $z/H = 0.1$, respectively (Fig. 14a). In fact, one more converging flow structure related to another low-speed region above the building array exists at $y/H \sim 16$, but this region is only detected by using a looser criterion (e.g., $\bar{u} = 7.5 \text{ m s}^{-1}$). In the NH case, the combination of low- and high-speed flow structures induces spanwise flow in the building array (detectable even in the time-averaged fields). In the BH case in which large-scale secondary circular flow dominates the whole model domain, one spanwise converging flow centered at $y/H = 23$ develops in the building array. The spanwise converging flow in



the BH case is stronger than that in the NH case, and it corresponds to the lower part of the secondary circular flow intensified by thermal updrafts. This thermally well-organized flow structure induces much stronger updrafts and much slower streamwise flow below the low-speed regions deep in the building array ($z/H = 0.1$) than low-speed flow structures in the NH case (Table 1). It is also noticeable that low-speed regions are centered over the building and cavity spaces and high-speed regions are centered over the streamwise-directed streets in both the NH and BH cases.

5. Summary and conclusions

Thermal effects on turbulent flow in and above a cubical building array were investigated using an LES model. No-heating and bottom-heating cases were simulated and compared with each other. In both the NH and BH cases, an instantaneous interface appears between the low- and high-speed air and parts of the interface are lifted or sunk by turbulent motions such as ejections and sweeps. In fact, the interface itself represents large-scale turbulent motions and the lifted parts of the interface correspond to the elongated low-speed regions and low-speed streaks above the building array and the sunken parts correspond to the high-speed streaks just above or below the rooftop height. The position and width of the turbulence coherent structures are dependent on the upper flow above them. For example, the lifted parts of the interface tend to expand more in the vertical direction below upper low-speed regions than below high-speed regions in both the NH and BH cases. In the conditionally averaged fields at $z/H = 3$, the elliptical structures of negative streamwise velocity perturbation and the vortical structures similar to hairpin vortices appear and the head part of the vortical structure expands more vertically when the street bottom is heated. The vertically expanded coherent structures represent well-organized and strengthened ejections in the BH case, and the strengthened ejections tend to occur in the shrunken low-speed regions compared with the NH case. While ejections are more important than sweeps in momentum transport at $z/H = 3$, the role of sweeps in momentum transport becomes important as the height approaches $z/H = 1$.

At or just above the rooftop height, sweeps are induced by sinking high-speed air or shear instability there

FIG. 13. Vertical profiles of 12 points-averaged (a) streamwise length scale of streamwise velocity, (b) spanwise length scale of spanwise velocity, and (c) streamwise length scale of vertical velocity over the IC points in the NH and BH cases.

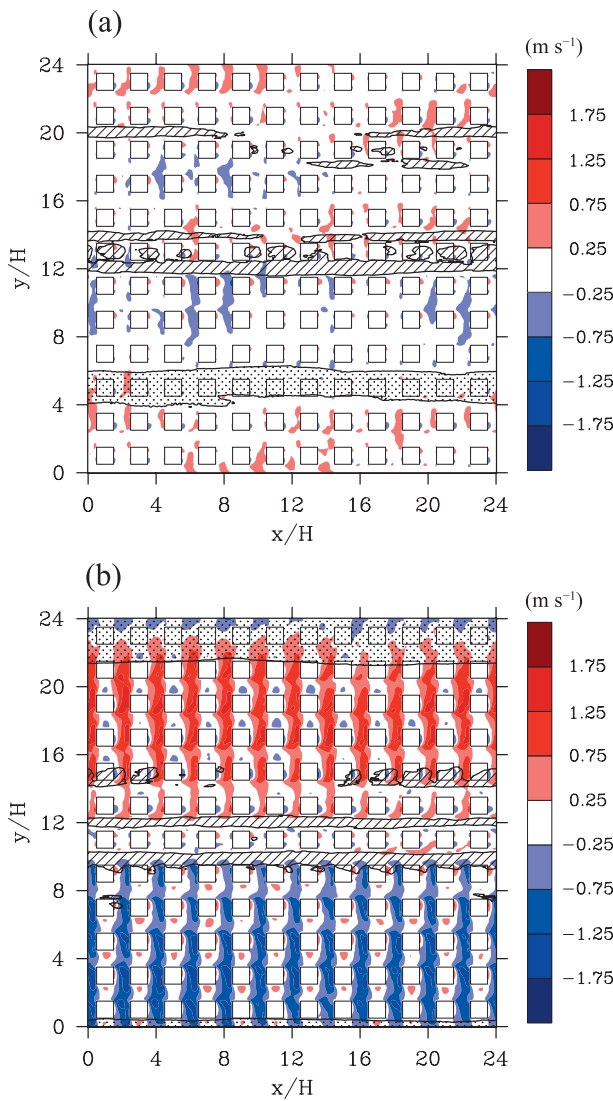


FIG. 14. Time-averaged spanwise velocity fields at $z/H = 0.1$ and the contours of equal streamwise velocity magnitude (6.0 m s^{-1} in the NH case and 5.5 m s^{-1} in the BH case) at $z/H = 3$ and the contours of equal streamwise velocity magnitude (4.4 m s^{-1} in the NH case and 4.9 m s^{-1} in the BH case) at $z/H = 1.2$ in the (a) NH and (b) BH cases. The dotted and hatched areas indicate low-speed regions at $z/H = 3$ and high-speed regions at $z/H = 1.2$.

and the sweeps transport more momentum downward than ejections in both the NH and BH cases. In the conditionally averaged fields, sweeps have a flat-disk shape at the tops of cavity spaces and a streamwise-elongated shape at the tops of intersection spaces in both the NH and BH cases. In the BH case, the shear layer at the tops of cavity spaces becomes thicker and the magnitude of vertical turbulent momentum flux is larger than in the NH case, partly because of ejections strengthened by bottom heating. In the intersection spaces in the NH and BH cases, turbulence coherent structures

composed of positive streamwise velocity perturbation and downdraft are obtained by conditional averaging and they induce spanwise diverging flow heading for nearby cavity spaces. Momentum in the intersection spaces is also transported into the nearby cavity spaces following the spanwise turbulent motions. Even in the time-averaged flow fields, spanwise flow is distinct in the building array and spanwise diverging and converging flows appear below the high- and low-speed regions, respectively. In the BH case, intensified secondary circular flow covering the whole model domain develops and it induces stronger and more organized spanwise flow in the building array, compared with the NH case.

It is noted that this study is primarily concerned with an idealized building array and a weakly unstable environment. Variations in building geometry and heating intensity can influence turbulent flow. Further study is required to investigate turbulent flow with different building geometries and heating intensities. It is known that scalar dispersion is well correlated with coherent structures in and above a building array (Coceal et al. 2007; Michioka et al. 2011). This deserves further study, particularly focusing on thermal effects.

Acknowledgments. The authors are grateful to three anonymous reviewers for providing valuable comments on this work. This work was supported by the National Research Foundation of Korea (NRF) grant funded by the Korea Ministry of Education, Science and Technology (MEST) (2012-0005674) and also supported by the Brain Korea 21 Project (through the School of Earth and Environmental Sciences, Seoul National University).

REFERENCES

- Adrian, R. J., C. D. Meinhart, and C. D. Tomkins, 2000: Vortex organization in the outer region of the turbulent boundary layer. *J. Fluid Mech.*, **422**, 1–54.
- Brown, M. J., R. E. Lawson, D. S. DeCroix, and R. L. Lee, 2001: Comparison of centerline velocity measurements obtained around 2D and 3D building arrays in a wind tunnel. Los Alamos National Laboratory Rep. LA-UR-01-4138, 7 pp.
- Castro, I. P., H. Cheng, and R. Reynolds, 2006: Turbulence over urban-like roughness: Deductions from wind-tunnel measurements. *Bound.-Layer Meteor.*, **118**, 109–131.
- Cheng, H., and I. P. Castro, 2002: Near wall flow over urban-like roughness. *Bound.-Layer Meteor.*, **104**, 229–259.
- Christen, A., M. W. Rotach, and R. Vogt, 2009: The budget of turbulent kinetic energy in the urban roughness sublayer. *Bound.-Layer Meteor.*, **131**, 193–222.
- Coceal, O., A. Dobre, and T. G. Thomas, 2007: Unsteady dynamics and organized structures from DNS over an idealized building canopy. *Int. J. Climatol.*, **27**, 1943–1953.
- Deardorff, J. W., 1980: Stratocumulus-capped mixed layers derived from a three-dimensional model. *Bound.-Layer Meteor.*, **18**, 495–527.

- Dubief, Y., and F. Delcayre, 2000: On coherent vortex identification in turbulence. *J. Turbul.*, **1**, 1–22.
- Fitzmaurice, L., R. H. Shaw, K. T. Paw U, and E. G. Patton, 2004: Three-dimensional scalar microfront systems in a large-eddy simulation of vegetation canopy flow. *Bound.-Layer Meteor.*, **112**, 107–127.
- Guala, M., S. E. Hommema, and R. J. Adrian, 2006: Large-scale and very-large-scale motions in turbulent pipe flow. *J. Fluid Mech.*, **554**, 521–542.
- Hutchins, N., and I. Marusic, 2007: Evidence of very long meandering features in the logarithmic region of turbulent boundary layers. *J. Fluid Mech.*, **579**, 1–28.
- Inagaki, A., and M. Kanda, 2010: Organized structure of active turbulence over an array of cubes within the logarithmic layer of atmospheric flow. *Bound.-Layer Meteor.*, **135**, 209–228.
- , M. C. L. Castillo, Y. Yamashita, M. Kanda, and H. Takimoto, 2012: Large-eddy simulation of coherent flow structures within a cubical canopy. *Bound.-Layer Meteor.*, **142**, 207–222.
- Kanda, M., 2006: Large-eddy simulations on the effects of surface geometry of building arrays on turbulent organized structures. *Bound.-Layer Meteor.*, **118**, 151–168.
- , R. Moriwaki, and F. Kasamatsu, 2004: Large-eddy simulation of turbulent organized structures within and above explicitly resolved cube arrays. *Bound.-Layer Meteor.*, **112**, 343–368.
- Kim, J.-J., and J.-J. Baik, 2004: A numerical study of the effects of ambient wind direction on flow and dispersion in urban street canyons using the RNG $k-\epsilon$ turbulence model. *Atmos. Environ.*, **38**, 3039–3048.
- Kim, K. C., and R. J. Adrian, 1999: Very large-scale motion in the outer layer. *Phys. Fluids*, **11**, 417–422.
- Letzel, M. O., M. Krane, and S. Raasch, 2008: High resolution urban large-eddy simulation studies from street canyon to neighbourhood scale. *Atmos. Environ.*, **42**, 8770–8784.
- Macdonald, R. W., R. F. Griffiths, and S. C. Cheah, 1997: Field experiments of dispersion through regular arrays of cubic structures. *Atmos. Environ.*, **31**, 783–795.
- Marusic, I., R. Mathis, and N. Hutchins, 2010: Predictive model for wall-bounded turbulent flow. *Science*, **329**, 193–196.
- Michioka, T., A. Sato, H. Takimoto, and M. Kanda, 2011: Large-eddy simulation for the mechanism of pollutant removal from a two-dimensional street canyon. *Bound.-Layer Meteor.*, **138**, 195–213.
- Piacsek, S. A., and G. P. Williams, 1970: Conservation properties of convection difference schemes. *J. Comput. Phys.*, **6**, 392–405.
- Raasch, S., and M. Schröter, 2001: PALM—A large-eddy simulation model performing on massively parallel computers. *Meteor. Z.*, **10**, 363–372.
- Raupach, M. R., 1981: Conditional statistics of Reynolds stress in rough-wall and smooth-wall turbulent boundary layers. *J. Fluid Mech.*, **108**, 363–382.
- Robinson, S. K., 1991: Coherent motions in the turbulent boundary layer. *Annu. Rev. Fluid Mech.*, **23**, 601–639.
- Rossi, R., D. A. Philips, and G. Iaccarino, 2010: A numerical study of scalar dispersion downstream of a wall-mounted cube using direct simulations and algebraic flux models. *Int. J. Heat Fluid Flow*, **31**, 805–819.
- Salizzoni, P., M. Marro, L. Soulac, N. Grosjean, and R. J. Perkins, 2011: Turbulent transfer between street canyons and the overlying atmospheric boundary layer. *Bound.-Layer Meteor.*, **141**, 393–414.
- Santiago, J. L., A. Martilli, and F. Martin, 2007: CFD simulation of airflow over a regular array of cubes. Part I: Three-dimensional simulation of the flow and validation with wind-tunnel measurements. *Bound.-Layer Meteor.*, **122**, 609–634.
- Uehara, K., S. Murakami, S. Oikawa, and S. Wakamatsu, 2000: Wind tunnel experiments on how thermal stratification affects flow in and above urban street canyons. *Atmos. Environ.*, **34**, 1553–1562.
- Watanabe, T., 2004: Large-eddy simulation of coherent turbulence structures associated with scalar ramps over plant canopies. *Bound.-Layer Meteor.*, **112**, 307–341.